

# Two-layer Thermally Driven Turbulence: Mechanisms for Interface Breakup

Hao-Ran Liu<sup>1</sup>, Kai Leong Chong<sup>1</sup>, Qi Wang<sup>1,2</sup>, Chong Shen Ng<sup>1</sup>,  
Roberto Verzicco<sup>3,4,1</sup> and Detlef Lohse<sup>1,5,†</sup>

<sup>1</sup>Physics of Fluids Group and Max Planck Center Twente for Complex Fluid Dynamics, MESA+Institute and J. M. Burgers Centre for Fluid Dynamics, University of Twente, P.O. Box 217, 7500AE Enschede, The Netherlands

<sup>2</sup>Department of Modern Mechanics, University of Science and Technology of China, Hefei 230027, China

<sup>3</sup>Dipartimento di Ingegneria Industriale, University of Rome “Tor Vergata”, Via del Politecnico 1, Roma 00133, Italy

<sup>4</sup>Gran Sasso Science Institute - Viale F. Crispi, 7 67100 L'Aquila, Italy

<sup>5</sup>Max Planck Institute for Dynamics and Self-Organization, Am Fassberg 17, 37077 Göttingen, Germany

(Received xx; revised xx; accepted xx)

It is commonly accepted that the breakup criteria of drops or bubbles in turbulence is governed by surface tension and inertia. However, also *buoyancy* can play an important role at breakup. In order to better understand this role, here we numerically study two-dimensional Rayleigh-Bénard convection for two immiscible fluid layers, in order to identify the effects of buoyancy on interface breakup. We explore the parameter space spanned by the Weber number  $5 \leq We \leq 5000$  (the ratio of inertia to surface tension) and the density ratio between the two fluids  $0.001 \leq \Lambda \leq 1$ , at fixed Rayleigh number  $Ra = 10^8$  and Prandtl number  $Pr = 1$ . At low  $We$ , the interface undulates due to plumes. When  $We$  is larger than a critical value, the interface eventually breaks up. Depending on  $\Lambda$ , two breakup types are observed: The first type occurs at small  $\Lambda \ll 1$  (e.g. air-water systems) when local filament thicknesses exceed the Hinze length scale. The second, strikingly different, type occurs at large  $\Lambda$  with roughly  $0.5 < \Lambda \leq 1$  (e.g. oil-water systems): The layers undergo a periodic overturning caused by buoyancy overwhelming surface tension. For both types the breakup, criteria can be derived from force balance arguments and show good agreement with the numerical results.

**Key words:**

## 1. Introduction

Liquid can break up or fragment in multiphase turbulence (Deane & Stokes 2002; Villiermaux 2007; Wang *et al.* 2019; Villiermaux 2020). This physical phenomenon is very important for raindrops (Villiermaux & Bossa 2009; Josserand & Zaleski 2003), for ocean waves and the resulting spray (Veron 2015), and even for the transmission of virus-laden droplets during coughing or sneezing (Bourouiba 2020; Chong *et al.* 2020). Once the physical mechanisms governing this important phenomenon are un-

† Email address for correspondence: d.lohse@utwente.nl

derstood, one can deduce quantitative criteria for the breakup to occur. In turbulence, for drops or bubbles the breakup criteria can be deduced from the balance of inertial and surface tension forces, as developed in the Kolmogorov-Hinze theory (Kolmogorov 1949; Hinze 1955). This theory well predicts the breakup criteria in experimental and numerical results in various flow systems, e.g., homogeneous isotropic turbulence (Martínez-Bazán *et al.* 1999; Perlekar *et al.* 2012; MuKolmogorov-Hinzeerjee *et al.* 2019), shear flows (Rosti *et al.* 2019), pipe flows (Hesketh *et al.* 1991) and ocean waves (Deane & Stokes 2002; Deike *et al.* 2016).

Whilst the classical Kolmogorov-Hinze theory considers only surface tension and inertial forces, in many multiphase turbulent flows also *buoyancy* can play an important role. Examples of multiphase buoyant turbulence include the hotspots and superswells in Earth’s mantle (Davaille 1999; Tackley 2000) and even flows during sneezing and exhalation (Bourouiba *et al.* 2014). In such flows, the breakup of the interface between the fluids is the key phenomenon. Yet, the exact mechanisms that drives interface breakup when buoyancy is crucial is unknown.

The objective of the present work is to shed light on this mechanism. As examples for turbulent flow where buoyancy is important and at the same time can easily be tuned, we take thermal convection, namely Rayleigh-Bénard (RB) convection (Ahlers *et al.* 2009; Lohse & Xia 2010; Chillà & Schumacher 2012) of two immiscible fluids. We numerically investigate the breakup mechanisms of the interface between the two immiscible fluids. The immiscible fluids are first arranged in two layers according to their densities and then heated from below and cooled from above. Most previous studies of such two-layer RB convection were conducted in the non-turbulent regime (Nataf *et al.* 1988; Prakash & Koster 1994; Busse & Petry 2009; Diwakar *et al.* 2014). Experimental studies in the turbulent regime were reported by Xie & Xia (2013), who focused on the flow structures in each layer and the coupling modes between the flows in the two layers, including viscous coupling and thermal coupling. Besides the classical rectangular/cylindrical configuration, the two-layer RB convection in spherical-shell geometry was also numerically studied by Yoshida & Hamano (2016). However, these previous studies only considered the case for strong surface tension, where the interface between the layers does not break up. In this study we will for the first time explore the case with interface breakup, which happens when surface tension is sufficiently small.

The control parameters of two-layer RB convection are the density ratio  $\Lambda$  between two fluids and the Weber number  $We$ , which is the ratio of inertia to surface tension. We will keep the Prandtl number  $Pr$  (a material property) and the Rayleigh number  $Ra$  (the dimensionless temperature difference between the plates) fixed, at values allowing for considerable turbulence. Our main result will be the phase diagram in the parameter space  $(We, \Lambda)$ , in which we identify the non-breakup and breakup regimes. At increasing  $We$ , we observe two distinct types of interface breakup. At small  $\Lambda \ll 1$ , the mechanism is well-described by the Kolmogorov-Hinze theory. However, at large  $0.5 < \Lambda \leq 1$ , the breakup is dominated by a balance between buoyancy and surface tension forces, leading to a periodic overturning-type breakup.

The organization of this paper is as follows. The numerical methodology is introduced in Section 2. Then in Section 3, we validate our code by studying droplet fragmentation in thermal turbulence and favourably compare the results to the Kolmogorov-Hinze theory. The main results on the interface breakup in two-layer RB turbulence are presented in Section 4, including a discussion of the first and second types of interface breakup in Section 4.1 and Section 4.2, respectively, and the analysis of the critical Weber number for interface breakup in Section 4.3. We finalise and further discuss our findings in Section 5.

## 2. Methodology: Cahn-Hilliard approach coupled to finite difference scheme

In this study, we performed the simulations in a two-dimensional (2D) rectangular domain with aspect ratio  $\Gamma = 2$  (width divided by height). Although 2D RB convection is different from 3D one, it still captures many essential features thereof (van der Poel *et al.* 2013). The direct numerical simulations solver for the Navier-Stokes equations is a second-order finite-difference open source solver (Verzicco & Orlandi 1996; van der Poel *et al.* 2015), namely AFiD, which has been well validated and used to study various turbulent flows (Stevens *et al.* 2018; Zhu *et al.* 2018b; Blass *et al.* 2020; Wang *et al.* 2020a,b). To simulate multiphase turbulent flows, we combine AFiD with the phase-field method (Jacqmin 1999; Ding *et al.* 2007; Liu & Ding 2015), which has also been successfully applied to the interfacial (Liu *et al.* 2018; Zhu *et al.* 2017; Chen *et al.* 2018, 2020) and turbulent flows (Soligo *et al.* 2019a; Roccon *et al.* 2019).

We consider two immiscible fluid layers of the same volume placed in the domain, named fluid  $H$  for the heavier fluid initially at the bottom and fluid  $L$  for the lighter fluid initially at the top. The mathematically sharp interface between two fluids is modeled by a diffuse interface with finite thickness, and can be represented by contours of the volume fraction  $C$  of fluid  $H$ . The corresponding volume fraction of fluid  $L$  is  $1 - C$ . The evolution of  $C$  is governed by the Cahn-Hilliard equations,

$$\frac{\partial C}{\partial t} + \nabla \cdot (\mathbf{u}C) = \frac{1}{Pe} \nabla^2 \psi, \quad (2.1)$$

where  $\mathbf{u}$  is the flow velocity, and  $\psi = C^3 - 1.5C^2 + 0.5C - \text{Cn}^2 \nabla^2 C$  is the chemical potential. The Cahn number  $\text{Cn} = 0.75h/D$ , where  $h$  is the mesh size and  $D$  the domain height, and the Péclet number  $Pe = 0.9/\text{Cn}$  are set the same as in Liu *et al.* (2017); Li *et al.* (2020). To overcome the mass loss in the phase-field method, a correction method as proposed by Wang *et al.* (2015) is used. This correction method resembles that used in Soligo *et al.* (2019b) and exhibits good performance (see Section 3).

The motion of the fluids is governed by the Navier-Stokes equation, heat transfer equation and continuity,

$$\rho \left( \frac{\partial \mathbf{u}}{\partial t} + \mathbf{u} \cdot \nabla \mathbf{u} \right) = -\nabla P + \sqrt{\frac{Pr}{Ra}} \nabla \cdot [\mu (\nabla \mathbf{u} + \nabla \mathbf{u}^T)] + \mathbf{F}_{st} + \left( \rho \theta - \frac{\rho}{Fr} \right) \mathbf{j}, \quad (2.2)$$

$$\frac{\partial \theta}{\partial t} + \mathbf{u} \cdot \nabla \theta = \sqrt{\frac{1}{PrRa}} \frac{1}{\rho C_p} \nabla \cdot (k \nabla \theta), \quad (2.3)$$

$$\nabla \cdot \mathbf{u} = 0, \quad (2.4)$$

here given in non-dimensionalized form. We have used the material properties of fluid  $H$ , the domain height  $D$ , the temperature difference  $\Delta$  between plates, and the free-fall velocity  $U = \sqrt{\alpha g D \Delta}$  to make these equations dimensionless, where  $\alpha$  is the thermal expansion coefficient of fluid  $H$  and  $g$  the gravitational acceleration. Then we define  $\rho = C + \Lambda(1 - C)$  as the dimensionless density,  $P$  the dimensionless pressure,  $\mu$  the dimensionless dynamic viscosity,  $C_p$  the dimensionless specific heat capacity,  $k$  the dimensionless thermal conductivity,  $\mathbf{F}_{st} = 6\sqrt{2}\psi\nabla C/(\text{Cn} \text{ We})$  the dimensionless surface tension force,  $\theta$  the dimensionless temperature,  $\mathbf{j}$  the unit vector in vertical direction. The superscript  $T$  stands for the transpose. Note that  $\rho$ ,  $\mu$ ,  $C_p$  and  $k$  in general vary in space.

In thermal flows, the density also depends on the temperature, so the dimensional

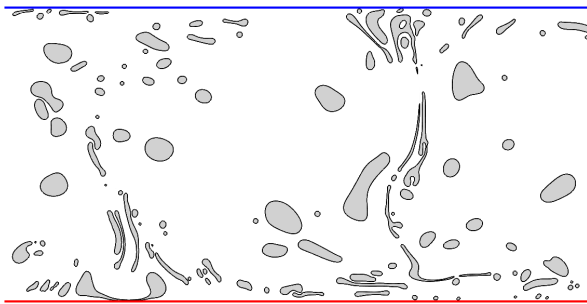


FIGURE 1. Snapshot with the advecting drops in Rayleigh-Bénard convection at density ratio  $\Lambda = 1$  and the system Weber number  $We = 16000$ . Drops are in gray, and the red and blue lines denote the plates with non-dimensional temperature  $\theta = 1$  and  $0$ , respectively. The corresponding movie is shown as Supplementary Material.

density is defined as  $\hat{\rho} = \hat{\rho}_H(T)C + \hat{\rho}_L(T)(1 - C)$ , where the subscripts  $H$  and  $L$  represent fluid  $H$  and fluid  $L$ , respectively, and  $\hat{\rho}_i(T) = [1 - \alpha(T - T_c)]\hat{\rho}_i(T_c)$  with  $T_c$  being the temperature on the top cold plate. Then we rewrite the dimensional density as  $\hat{\rho} = [\rho - \alpha(T - T_c)\rho]\hat{\rho}_H(T_c)$ . Further considering the Oberbeck-Boussinesq approximation in the Navier-Stokes equation (2.2), we have the dimensionless density  $\rho$  in the inertia term,  $\rho\theta$ , as the buoyancy term, and  $\rho/Fr$  as the gravity term, which cannot be ignored as in the single phase simulation, due to the different densities of the fluids. Furthermore, we only consider the case without phase transition.

The properties of fluid  $H$  and fluid  $L$  are set as follows: Their density ratio is  $\Lambda = \rho_L/\rho_H \leq 1$ . Except for the density  $\rho$ , all other properties of the two fluids are the same. The other dimensionless parameters are  $We = \rho_H U^2 D / \sigma$ ,  $Ra = \alpha g D^3 \Delta / (\nu \kappa)$ ,  $Pr = \nu / \kappa$ , the Froude number  $Fr = U^2 / (gD)$  (the ratio of inertia to gravity). Here  $\sigma$  is the surface tension coefficient,  $\nu = \mu / \rho$  the kinematic viscosity, and  $\kappa = k / (\rho C_p)$  the thermal diffusivity. We fix  $Ra = 10^8$ ,  $Pr = 1$ ,  $Fr = 1$  and  $\Gamma = 2$  (these values chosen to both ensure flows in the turbulent regime and simplify the simulations), and only vary  $We$  from 5 to 5000 and  $\Lambda$  from 0.001 (e.g. air-water system) to 1 (e.g. oil-water system).

The boundary conditions at the top and bottom plates are set as  $\partial C / \partial \mathbf{j} = 0$ ,  $\mathbf{j} \cdot \nabla \psi = 0$ , no-slip velocities and fixed temperature  $\theta = 0$  (top) and 1 (bottom). Periodic conditions are used in the horizontal direction. All the simulations begin with the same initial velocity and temperature fields, which originates from a well developed turbulent flow at  $We = 5$  and  $\Lambda = 1$ . Uniform grids with  $1000 \times 500$  gridpoints are used, which are sufficient for  $Ra = 10^8$  and  $Pr = 1$ , consistent with the grid resolution checks in Zhang *et al.* (2017). The details of the discretizations can be found in Ding *et al.* (2007); Verzicco & Orlandi (1996); M. S. Dodd (2014).

### 3. Droplet fragmentation in turbulent flow

We have verified our code against the existing theory from the literature. In this section RB convection with drops are simulated. Initially, the temperature field has a linear profile, the velocity field is set to 0, and a big drop of fluid  $H$  with a diameter of  $0.5D$  is placed at the center of the domain. The plates are superhydrophobic for fluid  $H$ , i.e.  $C = 0$  is used on both plates in the verification cases. We set  $\Lambda = 1$  and  $We$  from 2000 to 16000, and use uniform grids with  $2000 \times 1000$  gridpoints. Note that the value of  $We$  is large because it is a system Weber number, and the local Weber number of drops calculated from simulations is of the order of 1.

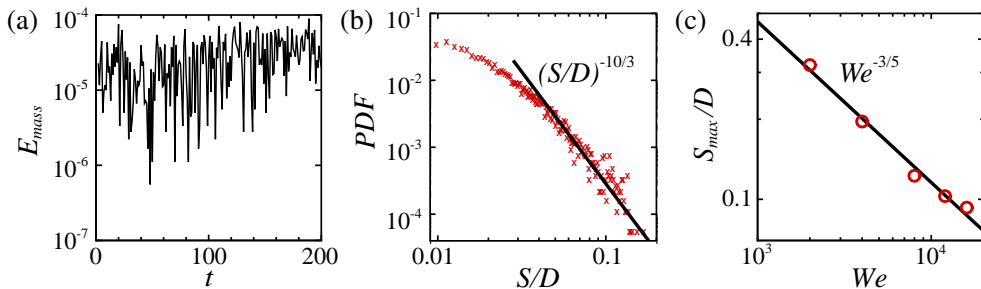


FIGURE 2. (a) Temporal evolution of Mass error  $E_{mass}$  and (b) probability density function (PDF) of the drop size  $S/D$  at  $We = 16000$ , where  $D$  is the domain height and  $S = 2\sqrt{A/\pi}$  with  $A$  being the drop area. (c) Maximal drop size  $S_{max}/D$  as function of  $We$ , where  $S_{max}$  is measured in the same way as in Hinze (1955), that is the diameter of the equivalent drop occupying 95% of the total dispersed area.

From the snapshot with the advecting drops in figure 1, we observe the large scale circulation, which is well known from single phase convection (Krishnamurti & Howard 1981; Xi *et al.* 2004; Zhu *et al.* 2018a; Xie *et al.* 2018). Figure 2(b) displays the distribution of the drop size  $S$ , which follows the scaling law  $(S/D)^{-10/3}$  (Garrett *et al.* 2000; Yu *et al.* 2020) valid for large drops. This scaling is consistent with experimental and other numerical results where the breakup of waves (Deane & Stokes 2002; Deike *et al.* 2016) or of a big drop (MuKolgogorov-Hinzeerjee *et al.* 2019) was studied. Moreover, the maximal size of drops  $S_{max}$  (see figure 2c) well agrees with the Kolmogorov-Hinze scaling law  $S_{max}/D \sim We^{-3/5}$ , which originates from Hinze (1955),

$$S_{Hinze} \sim \left( \frac{\sigma}{\rho} \right)^{\frac{3}{5}} \epsilon^{-\frac{2}{5}}, \quad (3.1)$$

where  $S_{Hinze}$  is the Hinze length scale and  $\epsilon$  the energy dissipation rate of the turbulent flow. In the Kolmogorov-Hinze theory, one assumption is that the local Weber number defined by the size and velocity of the drops adjusts such that it is  $We_{local} \sim O(1)$ . Indeed, in our simulations the local drop size adjusts correspondingly, so this assumption is fulfilled. The second assumption is that the flow exhibits inertial subrange scaling in the region of wave lengths comparable to the size of the largest drops. The spatial location where this assumption holds in RB convection is in the bulk region of convection (Lohse & Xia 2010). Therefore, the Kolmogorov-Hinze theory can indeed also be reasonably applied to 2D RB convection. At the same time the results show that the code and the approach give consistent results. Besides, figure 2(a) shows the temporal evolution of mass error  $E_{mass} = |M_t - M_0|/M_0$ , where  $M_t$  is the mass of fluid  $H$  at time  $t$  and  $M_0$  the initial mass. The results indicate good mass conservation.

#### 4. Interfacial breakup in two-layer turbulent thermal convection

In two-layer RB convection with an initially smooth interface between the two fluids (Xie & Xia 2013), the densities of the fluids depend on both  $\Lambda$  and the local temperature. At small  $\Lambda$ , for example, the air-water system with  $\Lambda = 0.001$ , fluid  $H$  (water) is always heavier than fluid  $L$  (air) even if fluid  $H$ , as the bottom layer, is hotter. In contrast, at large  $\Lambda$ , e.g., an oil-water system with  $\Lambda \approx 1$ , fluid  $H$  (water) is hotter than fluid  $L$  (oil), so it can be lighter. So depending on the value of  $\Lambda$  two distinct types of flow phenomena emerge.

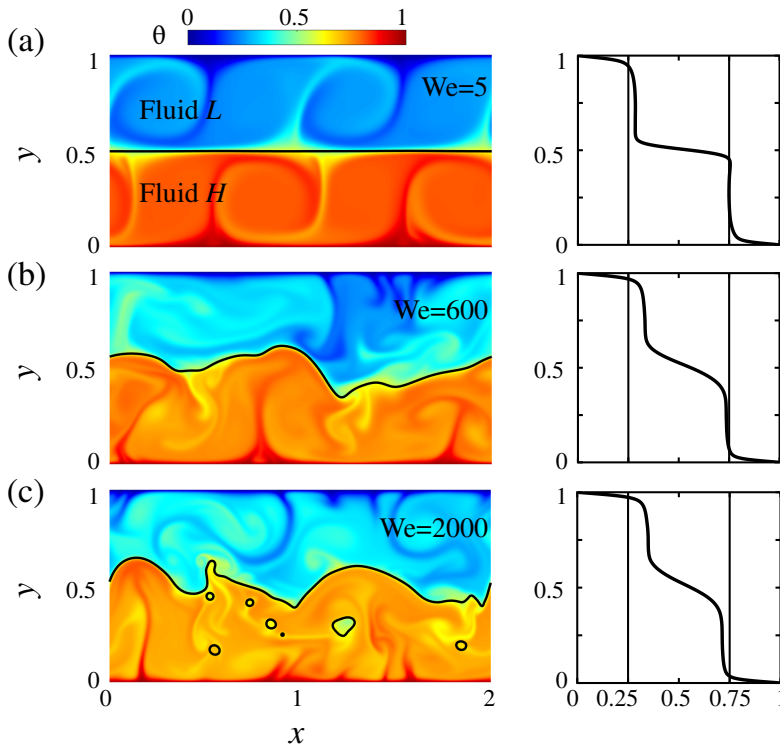


FIGURE 3. First type of interface breakup occurring for small  $\Lambda \ll 1$ : Temperature field and average temperature profile of two-layer Rayleigh-Bénard convection at  $\Lambda = 0.3$  for (a)  $We = 5$ , (b)  $We = 600$  and (c)  $We = 2000$ . The corresponding movies are shown as Supplementary Material.

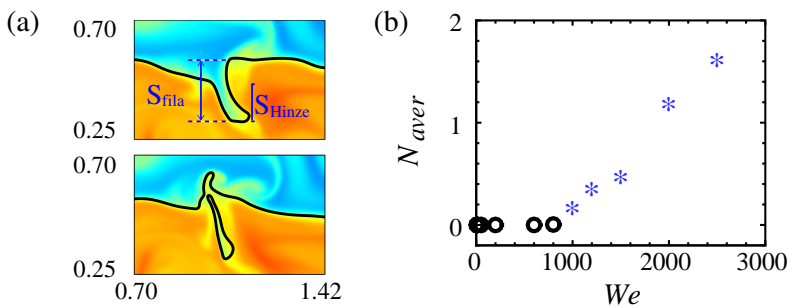


FIGURE 4. (a) Detachment process of a drop at  $We = 2000$ . (b) Time-averaged number of the drops of fluid  $L$  emerged in fluid  $H$  for various  $We$ , where the empty circles denote the non-breakup regime and stars the breakup regime.

#### 4.1. First type of interface breakup occurring for small $\Lambda \ll 1$

At small  $\Lambda$ , fluid  $H$  forms the bottom layer and fluid  $L$  the top one and large scale circulations are observed in each layer between the interface and the respective plate, as seen in figure 3(a). With increasing  $We$ , i.e. decreasing effects of surface tension compared to inertia, the interface becomes more unstable. At low  $We$  (figure 3a), the interface only slightly deforms because the surface tension is large enough to resist the inertia, such that the convection rolls are well-ordered. The temperature profile is similar to that



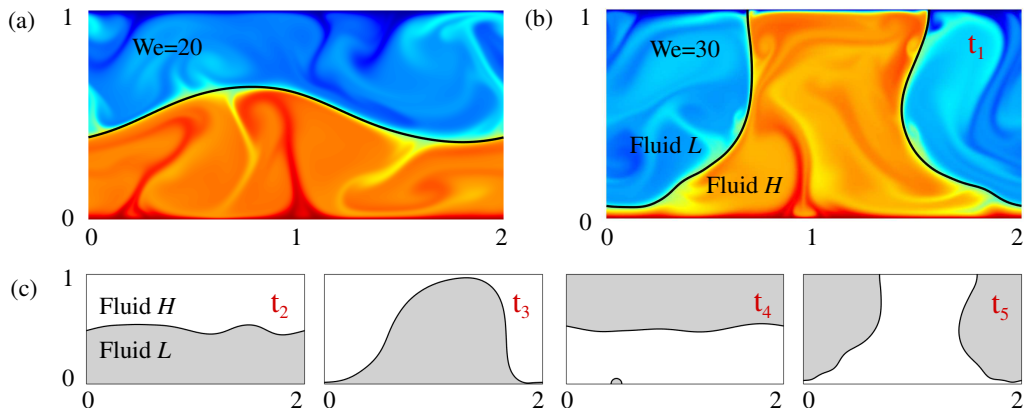


FIGURE 5. Second type of interface breakup occurring for large  $0.5 < \Lambda \leq 1$ : Snapshots at  $\Lambda = 0.8$  for two different  $We$ . (a) Wavy interface for  $We = 20$ . (b) Breakup and (c) overturning of interface for  $We = 30$  at different times  $t_1 = 617$ ,  $t_2 = 640$ ,  $t_3 = 661$ ,  $t_4 = 730$  and  $t_5 = 803$ .  $t_i$  are also marked in figure 6. The color map is the same as in figure 3. The corresponding movies are shown as Supplementary Material.

obtained from two-layer RB convection experiments (Davaille 1999). As  $We$  increases (figure 3b), the interface undulates due to the plumes. Each crest and trough on the interface is caused by a rising, or respectively settling plume in the heavier fluid  $H$ . In this situation, inertia is resisted by gravity together with surface tension. When  $We$  keeps increasing (figure 3c), the interface eventually breaks up and drops detach from the interface between two layers.

This “first type of interface breakup” (as we call it) occurs at small  $\Lambda$ . The process of the breakup begins from a settling plume in fluid  $H$  thanks to which the interface is pulled downwards, leading to a filament (or trough) on the interface (see figure 4a). If the filament length  $S_{fila}$  (defined in figure 4a) grows larger than the Hinze length scale  $S_{Hinze}$ , the filament will pinch off from the interface. Within the Kolmogorov-Hinze theory (Hinze 1955), the Hinze length scale  $S_{Hinze}$  in (3.1) is determined by the energy dissipation rate  $\epsilon$  of the turbulent flow. As seen from figure 3(c), more drops of fluid  $L$  exist in fluid  $H$  than of fluid  $H$  in fluid  $L$ . This finding resembles the breakup of the ocean waves (Deane & Stokes 2002), leading to more bubbles in water than drops in air. The reason is that  $S_{Hinze}$  is smaller in fluid  $H$  than in fluid  $L$  as  $\rho_H > \rho_L$ .

#### 4.2. Second type of interface breakup occurring for large $0.5 < \Lambda \leq 1$

We now come to the large  $\Lambda \approx 1$  case: Since fluid  $H$  carries hotter fluid than fluid  $L$ , due to thermal expansion it can become lighter than fluid  $L$ , inverting the original density contrast at equal temperature. In this situation, buoyancy drives fluid  $H$  upwards and fluid  $L$  downwards. This leads to wave crests and troughs, as shown in figure 5. If  $We$  is low (figure 5a), the surface tension can maintain a stable interface, though it is wobbling. However, if  $We$  increases (figure 5b), the wobbling wave on the interface can amplify more and more until it finally touches the upper and/or lower plate and breaks up. We call this type of interface breakup the “second type of breakup”.

For this second type of interface breakup, the breakup process is strikingly different from the first type. A periodic overturning is observed both in the fluid dynamics and in the heat transfer (see figure 5c and figure 6): After interface breakup at  $t_1$ , fluid  $H$  initially at the bottom gradually rises above fluid  $L$  and finally contacts the upper cold plate. The increased wetted area of the hotter fluid on the upper cold plate causes a

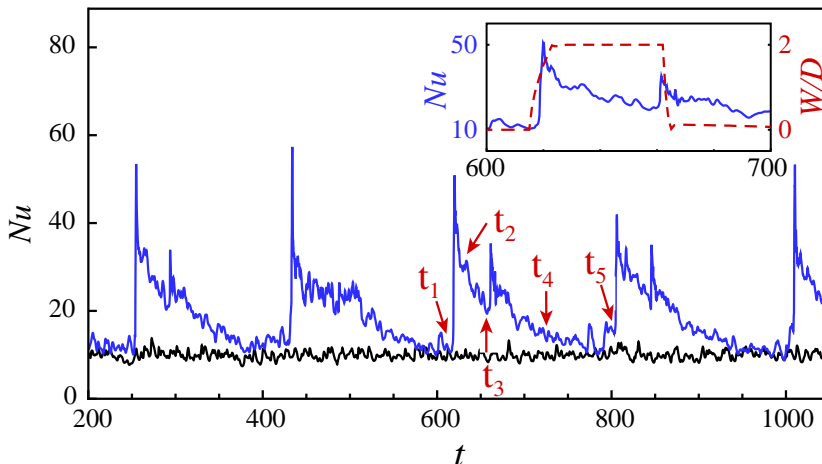


FIGURE 6. Temporal evolution of the Nusselt number  $Nu$  at the bottom plate for  $We = 20$  (black) and  $We = 30$  (blue). The inset shows a zoom of the temporal evolution of  $Nu$  for  $We = 30$  and the corresponding wetted length function  $W/D$  of fluid  $H$  at the top plate.

strong enhancement of the Nusselt number  $Nu$ , in the shown case 5 times of  $Nu$  without breakup, as shown in figure 6. Then, fluid  $H$  on the top gets cooler and thus heavier, while fluid  $L$  at the bottom warmer and thus lighter. Once again, the breakup occurs after  $t_3$  and the fluids swap their positions (see figure 5c). Since fluid  $L$  is lighter than fluid  $H$  at the same temperature, it is easier to rise and touch the cold plate. Thus, with fluid  $L$  as the bottom layer, the temperature of the bottom layer during the breakup is lower than that when fluid  $H$  is the bottom layer. This is also reflected in the heat transfer. The peak of  $Nu$  after  $t_3$  is smaller, only 3 times of  $Nu$  without breakup, and the preparation time for breakup from  $t_2$  to  $t_3$  is shorter than that from  $t_4$  to  $t_5$ .

#### 4.3. Critical Weber number for interface breakup

The full phase diagram in the parameter space  $(We, \Lambda)$  – revealing when and what regime occurs – is plotted in figure 7. When  $We$  is larger than a certain critical value  $We_c$ , which depends on  $\Lambda$ , the interface breaks up. It is noteworthy that the transition between the non-breakup and breakup regimes show two distinct trends, which correspond to the two above identified types of interface breakup, respectively. The natural question that arises here is then: What sets the critical value  $We_c$  at given  $\Lambda$ ?

In the first type of interface breakup (small  $\Lambda \ll 1$ ), detaching drops are generated from the initial interface when the filament length  $S_{fila}$  is of the order of the Hinze length scale  $S_{Hinze}$ .  $S_{fila}$  is estimated by analyzing the force balance: the sum of gravity and surface tension force counteracts the inertial force,

$$\delta\rho g S_{fila} + \frac{\sigma}{S_{fila}} \sim \rho_H U_H^2, \quad (4.1)$$

where  $U_H = \sqrt{\alpha g (D/2) (\Delta/2)}$  and  $\delta\rho$  is the density difference from the bottom (fluid  $H$ ) to the top (fluid  $L$ ) of the filament. We define  $\delta\rho = \rho_H(T_H) - \rho_L(T_L)$ , where  $T_i$  is the temperature of fluid  $i$ . We further found that the value of gravity is one order of magnitude greater than surface tension based on the data of cases near the transition region in the first type. This indicates that the generation of the filament is dominated by gravity and inertia. Therefore we neglect the term  $\sigma/S_{fila}$  in (4.1). Note however that the



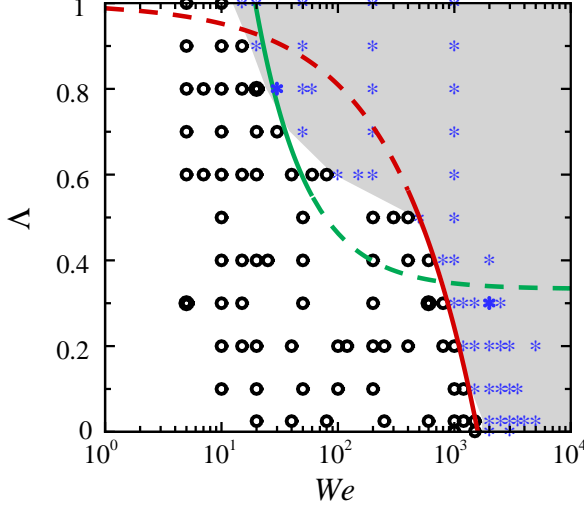


FIGURE 7. Phase diagram in the  $We-\Lambda$  parameter space. Empty circles denote the non-breakup regime and stars the interface breakup regime. Symbols with boldface are the cases shown in figure 3 and 5. The gray shadow is a guide to the eye. The red and green lines denote the criteria, (4.3) with prefactor 1590 and (4.6) with prefactor 13.3, for the first and second type of interface breakup, respectively. The solid parts of the lines, where the theory is supposed to hold, indeed nicely agree with the numerical results.

surface tension force still plays an important role to determine  $S_{Hinze}$  in (3.1). Combining (4.1), (3.1) and the exact relation  $\epsilon = \nu^3/D^4 (Nu-1)RaPr^{-2}$  (Shraiman & Siggia 1990; Ahlers *et al.* 2009), the dimensionless form of  $S_{fila} \sim S_{Hinze}$  yields

$$\left[ \left( \frac{1}{Fr} - \theta_H \right) - \Lambda \left( \frac{1}{Fr} - \theta_L \right) \right]^{-1} \sim We_c^{-\frac{3}{5}} \left( \frac{Nu-1}{\sqrt{RaPr}} \right)^{-\frac{2}{5}}, \quad (4.2)$$

with the non-dimensional temperatures  $\theta_i = (T_i - T_c)/\Delta$  with  $i$  being  $H$  and  $L$ .  $\theta_H$  and  $\theta_L$  are both taken as 0.5 given that the filament is generated near the interface, where the temperature is 0.5. To further simplify (4.2),  $Nu$  is regarded as constant because the simulation data show that  $Nu$  varies only within 15% in the non-breakup regime. Given that the  $Nu$ ,  $Ra$ ,  $Pr$  and  $Fr$  are all constant, the criteria for the first type of interface breakup simplifies to

$$We_c \sim (1 - \Lambda)^{\frac{5}{3}}. \quad (4.3)$$

In the second type of interface breakup (large  $\Lambda \approx 1$ ), the hot fluid  $H$  is lighter than the cold fluid  $L$ , so the buoyancy caused by the unstable temperature stratification can overcome the surface tension, leading to waves on the interface. The buoyancy acting on the wave originates from the density difference between the fluid above and below the wobbling interface (see figure 5). The balance is described by

$$[\rho_L(T_L) - \rho_H(T_H)]gD \sim \frac{\sigma}{D}, \quad (4.4)$$

where  $T_i$  is the average temperature in the bulk of fluid  $i$ , and the interface deformation is of the order of  $D$  because the breakup occurs when the wave amplitude is larger than half of the plate distance  $D$ , thus that the interface touches the plates (see figure 5b).

The dimensionless form of (4.4) reads

$$\Lambda \left( \frac{1}{Fr} - \theta_L \right) - \left( \frac{1}{Fr} - \theta_H \right) \sim \frac{1}{We_c}. \quad (4.5)$$

From the temperature profile in figure 3, we estimate  $\theta_H = 0.75$  and  $\theta_L = 0.25$ . Then (4.5) simplifies to

$$We_c \sim \left( \Lambda - \frac{1}{3} \right)^{-1}. \quad (4.6)$$

Figure 7 shows that (4.3) and (4.6) indeed well describe the scaling relations of transitions between the non-breakup and breakup regimes.

In the breakup regimes at large  $\Lambda \sim 1$ , as  $We$  increases, the periodically overturning of fluid layers gradually becomes chaotic with more and more drops generated from the breakup of the interface. Eventually, the flow pattern is determined by the advection of the small drops (figure 1). There is no clear boundary in the parameter space for this transition and it happens over a considerable range in parameter space. Therefore, in this study, we only focus on when and how the breakup occurs.

## 5. Conclusions

In summary, we have numerically shown two distinct types of interface breakup in two-layer RB convection, which result from different dominant forces. At small  $\Lambda \ll 1$ , a filament is generated on the interface due to the competition of inertial force and buoyancy. The interface breaks up in the form of filament detachment when the local filament thicknesses exceed the Hinze length scale. At large  $\Lambda$  with roughly  $0.5 < \Lambda \leq 1$ , the periodic overturning-type breakup is caused by buoyancy overwhelming surface tension. From the force balance arguments above, we derive the breakup criteria for two types, respectively. Our approaches show good agreements with the numerical results.

The threshold of regimes in this work is derived from a force balance argument, which is not limited to 2D. For 3D, of course, some expressions need to be modified, for example, surface tension force from  $F_{st} = \sigma/R$  in 2D to  $F_{st} = \sigma(1/R_1 + 1/R_2)$  in 3D. Besides, we also note that previous studies also showed that 2D and 3D Rayleigh-Bénard convection have similar features for  $Pr \geq 1$ , see [van der Poel \*et al.\* \(2013\)](#). Therefore, we expect our results from 2D flow could be directly extended to 3D flow.

Our findings clearly demonstrate that interface breakup in multilayer thermally driven turbulence cannot be solely described by the Kolmogorov-Hinze theory, which is only applicable when the lower layer is much denser than the upper layer or when thermal expansion effects do not play a role. Interestingly, when the lower layer is less dense than the upper layer, the system is unstably stratified, leading to the new breakup type described in this paper where buoyancy and surface tension are the dominant forces. It would be interesting to test our predictions of (4.2) and (4.5) for the transitions between the different regimes in a larger range of the control parameters  $Ra$ ,  $Pr$ , and  $Fr$ , which were kept fixed here. More generally, our findings emphasize the role of buoyancy in interfacial breakup. Clearly, buoyancy will also play a prominent role in the interfacial breakup in other turbulent flows, such as Bénard-Marangoni convection, and horizontal and vertical convection. All these phenomena add to the richness of physicochemical hydrodynamics of droplets far from equilibrium ([Lohse & Zhang 2020](#)).

## Acknowledgments

The work was financially supported by ERC-Advanced Grant under the project no. 740479. We acknowledge PRACE for awarding us access to MareNostrum in Spain at the Barcelona Computing Center (BSC) under the project 2018194742. This work was also carried out on the national e-infrastructure of SURFsara, a subsidiary of SURF cooperation, the collaborative ICT organization for Dutch education and research.

## Declaration of interests

The authors report no conflict of interest.

## Supplementary movies

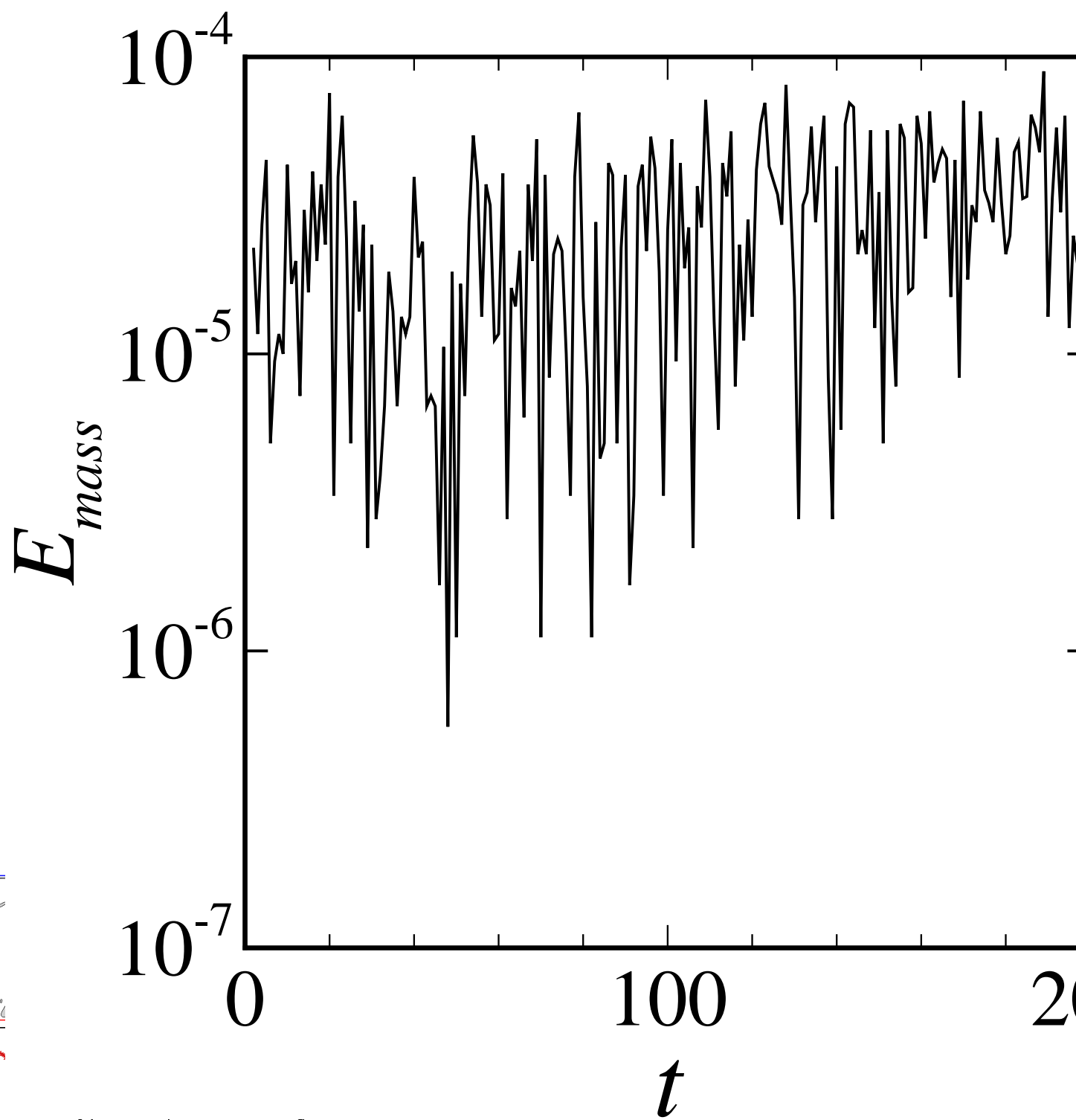
Supplementary movies are available at [URL](#)

## REFERENCES

- AHLERS, G., GROSSMANN, S. & LOHSE, D. 2009 Heat transfer and large scale dynamics in turbulent Rayleigh-Bénard convection. *Rev. Mod. Phys.* **81**, 503.
- BLASS, A., ZHU, X., VERZICCO, R., LOHSE, D. & STEVENS, R. J.A.M. 2020 Flow organization and heat transfer in turbulent wall sheared thermal convection. *J. Fluid Mech.* **897**, A22.
- BOUROUBA, L. 2020 Turbulent gas clouds and respiratory pathogen emissions: Potential implications for reducing transmission of covid-19. *JAMA* .
- BOUROUBA, L., DEHANDSCHOEWERCKER, E. & BUSH, J. W. M. 2014 Violent expiratory events: on coughing and sneezing. *J. Fluid Mech.* **745**, 537–563.
- BUSSE, F. H. & PETRY, M. 2009 Homologous onset of double layer convection. *Phys. Rev. E* **80**, 046316.
- CHEN, H., LIU, H.-R., GAO, P. & DING, H. 2020 Submersion of impacting spheres at low Bond and Weber numbers owing to a confined pool. *J. Fluid Mech.* **884**, A13.
- CHEN, H., LIU, H.-R., LU, X.-Y. & DING, H. 2018 Entrapping an impacting particle at a liquid-gas interface. *J. Fluid Mech.* **841**, 1073–1084.
- CHILLÀ, F. & SCHUMACHER, J. 2012 New perspectives in turbulent Rayleigh-Bénard convection. *Eur. Phys. J. E* **35**, 58.
- CHONG, K. L., NG, C. S., HORI, N., YANG, R., VERZICCO, R. & LOHSE, D. 2020 Extended lifetime of respiratory droplets in a turbulent vapour puff and its implications on airborne disease transmission. *arXiv preprint arXiv:2008.01841* .
- DAVAILLE, A. 1999 Simultaneous generation of hotspots and superswells by convection in a heterogeneous planetary mantle. *Nature* **402**, 756–760.
- DEANE, G. B. & STOKES, M. D. 2002 Scale dependence of bubble creation mechanisms in breaking waves. *Nature* **418**, 839–844.
- DEIKE, L., MELVILLE, W. K. & POPINET, S. 2016 Air entrainment and bubble statistics in breaking waves. *J. Fluid Mech.* **801**, 91–129.
- DING, H., SPELT, P. D. M. & SHU, C. 2007 Diffuse interface model for incompressible two-phase flows with large density ratios. *J. Comput. Phys.* **226**, 2078–2095.
- DIWAKAR, S. V., TIWARI, S., DAS, S. K. & SUNDARARAJAN, T. 2014 Stability and resonant wave interactions of confined two-layer Rayleigh-Bénard systems. *J. Fluid Mech.* **754**, 415–455.
- GARRETT, C., LI, M. & FARMER, D. 2000 The connection between bubble size spectra and energy dissipation rates in the upper ocean. *J. Phys. Oceanogr.* **30** (9), 2163–2171.
- HESKETH, R. P., ETCHELLS, A. W. & RUSSELL, T. W. F. 1991 Bubble breakage in pipeline flow. *Chem. Eng. Sci.* **46** (1), 1–9.
- HINZE, J. O. 1955 Fundamentals of the hydrodynamic mechanism of splitting in dispersion processes. *AIChE J.* **1** (3), 289–295.
- JACQMIN, D. 1999 Calculation of two-phase Navier-Stokes flows using Phase-Field modeling. *J. Comput. Phys.* **155**, 96–127.

- JOSSERAND, C. & ZALESKI, S. 2003 Droplet splashing on a thin liquid film. *Phys. Fluids* **15**, 1650.
- KOLMOGOROV, A. N. 1949 On the disintegration of drops in a turbulent flow. *Dokl. Akad. Nauk. SSSR* **66**, 825–828.
- KRISHNAMURTI, R. & HOWARD, L. N. 1981 Large-scale flow generation in turbulent convection. *Proc. Natl. Acad. Sci. USA* **78** (4), 1981–1985.
- LI, H.-L., LIU, H.-R. & DING, H. 2020 A fully 3d simulation of fluid-structure interaction with dynamic wetting and contact angle hysteresis. *J. Comput. Phys.* **420**, 109709.
- LIU, H.-R. & DING, H. 2015 A diffuse-interface immersed-boundary method for two-dimensional simulation of flows with moving contact lines on curved substrates. *J. Comput. Phys.* **294**, 484–502.
- LIU, H.-R., GAO, P. & DING, H. 2017 Fluid-structure interaction involving dynamic wetting: 2D modeling and simulations. *J. Comput. Phys.* **348**, 45–65.
- LIU, H.-R., ZHANG, C.-Y., GAO, P., LU, X.-Y. & DING, H. 2018 On the maximal spreading of impacting compound drops. *J. Fluid Mech.* **854**, R6.
- LOHSE, D. & XIA, K.-Q. 2010 Small-scale properties of turbulent Rayleigh-Bénard convection. *Annu. Rev. Fluid Mech.* **42**, 335.
- LOHSE, D. & ZHANG, X. 2020 Physicochemical hydrodynamics of droplets out of equilibrium. *Nat. Rev. Phys.* **2**, 426–443.
- M. S. DODD, A. FERRANTE 2014 A fast pressure-correction method for incompressible two-fluid flows. *J. Comput. Phys.* **273**, 416–434.
- MARTÍNEZ-BAZÁN, C., MONTAÑÉS, J. L. & LASHERAS, J. C. 1999 On the breakup of an air bubble injected into a fully developed turbulent flow. Part 2. Size PDF of the resulting daughter bubbles. *J. Fluid Mech.* **401**, 183–207.
- MUKOLMOGOROV-HINZEERJEE, S., SAFDARI, A., SHARDT, O., KENJEREŠ, S. & VAN DEN AKKER, H. E. A. 2019 Droplet-turbulence interactions and quasi-equilibrium dynamics in turbulent emulsions. *J. Fluid Mech.* **878**, 221–276.
- NATAF, H. C., MORENO, S. & CARDIN, P. 1988 What is responsible for thermal coupling in layered convection? *J. Phys. (Paris)* **49**, 1707–1714.
- PERLEKAR, P., BIFERALE, L., SBRAGAGLIA, M., SRIVASTAVA, S. & TOSCHI, F. 2012 Droplet size distribution in homogeneous isotropic turbulence. *Phys. Fluids* **24**, 065101.
- PRAKASH, A. & KOSTER, J. N. 1994 Convection in multiple layers of immiscible liquids in a shallow cavity I. steady natural convection. *Intl J. Multiphase Flow* **20** (2), 383–396.
- ROCCON, A., ZONTA, F. & SOLDATI, A. 2019 Turbulent drag reduction by compliant lubricating layer. *J. Fluid Mech.* **863**, R1.
- ROSTI, M. E., GE, Z., JAIN, S. S., DODD, M. S. & BRANDT, L. 2019 Droplets in homogeneous shear turbulence. *J. Fluid Mech.* **876**, 962–984.
- SHRAIMAN, B. I. & SIGGIA, E. D. 1990 Heat transport in high rayleigh number convection. *Phys. Rev. A* **42**, 3650–3653.
- SOLIGO, G., ROCCON, A. & SOLDATI, A. 2019a Breakage, coalescence and size distribution of surfactant-laden droplets in turbulent flow. *J. Fluid Mech.* **881**, 244–282.
- SOLIGO, G., ROCCON, A. & SOLDATI, A. 2019b Mass-conservation-improved phase field methods for turbulent multiphase flow simulation. *Acta Mech.* **230**, 683–696.
- STEVENS, R. J. A. M., BLASS, A., ZHU, X., VERZICCO, R. & LOHSE, D. 2018 Turbulent thermal superstructures in Rayleigh-Bénard convection. *Phys. Rev. Fluids* **3**, 041501.
- TACKLEY, P. J. 2000 Mantle convection and plate tectonics: Toward an integrated physical and chemical theory. *Science* **288**, 2002–2007.
- VAN DER POEL, E. P., OSTILLA-MÓNICO, R., DONNERS, J. & VERZICCO, R. 2015 A pencil distributed finite difference code for strongly turbulent wall-bounded flows. *Comput. Fluids* **116**, 10.
- VAN DER POEL, E. P., STEVENS, R. J. A. M. & LOHSE, D. 2013 Comparison between two- and three-dimensional Rayleigh-Bénard convection. *J. Fluid Mech.* **736**, 177–194.
- VERON, F. 2015 Ocean spray. *Annu. Rev. Fluid Mech.* **47**, 507–38.
- VERZICCO, R. & ORLANDI, P. 1996 A finite-difference scheme for three-dimensional incompressible flows in cylindrical coordinates. *J. Comput. Phys.* **123**, 402.
- VILLERMAUX, E. 2007 Fragmentation. *Annu. Rev. Fluid Mech.* **39**, 419–46.
- VILLERMAUX, E. 2020 Fragmentation versus cohesion. *J. Fluid Mech.* **898**, P1.

- VILLERMAUX, E. & BOSSA, B. 2009 Single-drop fragmentation determines size distribution of raindrops. *Nature Phys.* **5**, 697–702.
- WANG, Q., CHONG, K. L., STEVENS, R. J. A. M., VERZICCO, R. & LOHSE, D. 2020*a* From zonal flow to convection rolls in Rayleigh–Bénard convection with free-slip plates. *J. Fluid Mech.* **905**, A21.
- WANG, Q., VERZICCO, R., LOHSE, D. & SHISHKINA, O. 2020*b* Multiple states in turbulent large-aspect ratio thermal convection: What determines the number of convection rolls? *Phys. Rev. Lett.* **125**, 074501.
- WANG, Y., SHU, C., SHAO, J.-Y., WU, J. & NIU, X.-D. 2015 A mass-conserved diffuse interface method and its application for incompressible multiphase flows with large density ratio. *J. Comput. Phys.* **290**, 336–351.
- WANG, Z., MATHAI, V. & SUN, C. 2019 Self-sustained biphasic catalytic turbulence. *Nat. Commun.* **10**, 3333.
- XI, H.-D., LAM, S. & XIA, K.-Q. 2004 From laminar plumes to organized flows: the onset of large-scale circulation in turbulent thermal convection. *J. Fluid Mech.* **503**, 47–56.
- XIE, Y.-C., DING, G. Y. & XIA, K.-Q. 2018 Flow topology transition via global bifurcation in thermally driven turbulence. *Phys. Rev. Lett.* **120**, 214501.
- XIE, Y.-C. & XIA, K.-Q. 2013 Dynamics and flow coupling in two-layer turbulent thermal convection. *J. Fluid Mech.* **728**, R1.
- YOSHIDA, M. & HAMANO, Y. 2016 Numerical studies on the dynamics of two-layer Rayleigh–Bénard convection with an infinite Prandtl number and large viscosity contrasts. *Phys. Fluids* **28**, 116601.
- YU, X., HENDRICKSON, K. & YUE, D. K. P. 2020 Scale separation and dependence of entrainment bubble-size distribution in free-surface turbulence. *J. Fluid Mech.* **885**, R2.
- ZHANG, Y., ZHOU, Q. & SUN, C. 2017 Statistics of kinetic and thermal energy dissipation rates in two-dimensional turbulent Rayleigh–Bénard convection. *J. Fluid Mech.* **814**, 165–184.
- ZHU, X., MATHAI, V., STEVENS, R. J. A. M., VERZICCO, R. & LOHSE, D. 2018*a* Transition to the ultimate regime in two-dimensional Rayleigh–Bénard convection. *Phys. Rev. Lett.* **120**, 144502.
- ZHU, X., VERSCHOOF, R., BAKOLMOGOROV-HINZEUIS, D., HUISMAN, S. G., VERZICCO, R., SUN, C. & LOHSE, D. 2018*b* Wall roughness induces asymptotic ultimate turbulence. *Nature Phys.* **14**, 417–423.
- ZHU, Y., LIU, H.-R., MU, K., GAO, P. & DING, H. 2017 Dynamics of drop impact onto a solid sphere: spreading and retraction. *J. Fluid Mech.* **824**, R3.



(a)



(b)

